Can large strains be accommodated by small faults: "Brittle flow of rocks" revised

Xiaoyu Zou[1], **Yuri Fialko**[1]

[1]Institute of Geophysics and Planetary Physics, Scripps Institution of Oceanography, University of California San Diego, La Jolla, CA 92093, USA.

Key Points:

- We analyze the fault length-frequency distribution in developing (structurally immature) fault systems.
- The cumulative frequency distribution follows a power law over a range of fault lengths spanning 8 orders of magnitude, with a negative power-law exponent of $\sim$2, implying scale independence.
- Small faults within the brittle upper crust can accommodate a substantial ($> 30\%$) fraction of tectonic strain.

Corresponding author: Xiaoyu Zou, x3zou@ucsd.edu

Abstract

Brittle deformation in the upper crust is thought to occur primarily via faulting. The fault length-frequency distribution determines how much deformation is accommodated by numerous small faults vs a few large ones. To evaluate the amount of deformation due to small faults, we analyze the fault length distribution using high-quality fault maps spanning a wide range of spatial scales from a laboratory sample to an outcrop to a tectonic domain. We find that the cumulative fault length distribution is well approximated by a power law with a negative exponent close to 2. It follows that faulting is a self-similar process, and a substantial fraction of tectonic strain can be accommodated by faults that don't cut through the entire brittle layer, consistent with inferences of "hidden strain" from natural and laboratory observations. A continued accumulation of tectonic strain may eventually result in a transition from self-similar fault networks to localized mature faults.

Plain language summary

The Earth's crust is pervasively damaged, and contains faults of various sizes and orientations. We use mapped fault traces from multiple data sets spanning a wide range of scales to investigate how much deformation is accommodated by small vs large faults. The fault length distribution is often assumed to be fractal, i.e., following a power law. The power-law exponent α quantifies the relative contributions of many small faults relative to a few large ones. For $\alpha \leq 1$, the contribution of small faults is negligible, while for $\alpha \geq 2$, strains accommodated by small faults become significant. We find that the cumulative fault length distribution approximately follows a power law with an exponent close to 2. This implies that small faults in developing shear zones can accommodate substantial tectonic strain.

Introduction

Tectonic deformation in the brittle upper crust is mainly accommodated by faulting (e.g., S. Cox & Scholz, 1988). Faults are ubiquitous in both intraplate settings and at plate boundaries (e.g, Ojo et al., 2022; R. T. Cox et al., 2001; Rui & Stamps, 2019; Bürgmann & Pollard, 1994). As faults continue to slip, they increase their length via crack tip propagation, linkage, and coalescence (e.g., Mansfield & Cartwright, 2001; S. Cox & Scholz, 1988; Dawers & Anders, 1995; Fossen, 2020; Rotevatn et al., 2019). As a result,

the upper crust contains faults of various sizes, from millimeter-long microfractures to mature faults extending hundreds of kilometers. The fault length distribution controls the relative contributions of small vs large faults to a total strain budget and is of interest to many disciplines including tectonics, engineering geology, hydrogeology, petroleum industry, and seismic hazards assessment (e.g., C. H. Scholz & Cowie, 1990; Louderback, 1950; Bense et al., 2013; Bonnet et al., 2001).

Previous studies suggested a variety of functional forms describing the fault size distribution. It is generally believed that in a low-strain environment (e.g., developing shear zones), fault populations are fractal and thus follow a power-law distribution (e.g., Childs et al., 1990; Turcotte, 1986; Bour & Davy, 1999; Bonnet et al., 2001; Ben-Zion & Sammis, 2003). Nicol et al. (1996) noted that the fault length distribution may deviate from a power-law if a wide range of fault lengths is considered, and that the power-law exponent may vary at the low end of the fault length distribution owing to spatial clustering. In contrast, Odling et al. (1999) argued that the fault length distribution may appear as log-normal in individual data sets with a given detection threshold, but is a power-law for "composite" data sets that combine a number of individual data sets spanning a wide range of spatial scales. Gupta and Scholz (2000) suggested a transition from a power-law to an exponential distribution when tectonic strain exceeds a critical threshold of the order of 0.1.

In case of a power-law distribution, the number of faults N that have lengths greater than or equal to L is given by

$$N(L) = CL^{-\alpha} \tag{1}$$

where C is an empirical constant, and $\alpha > 0$ is an absolute value of the power-law exponent, also known as the Pareto index (e.g., Clark et al., 1999). The derivative of the cumulative fault length distribution (1) with respect to L is the probability density,

$$\frac{dN}{dL} = C(1-\beta)L^{-\beta}, \tag{2}$$

which is also a power law, with $\beta = \alpha + 1$. The probability density (2) is sometimes referred to as the non-cumulative frequency distribution. A number of studies used field observations to test the assumption of a fractal distribution, and estimate parameters C and α (or β). Reported values of the best-fit power-law exponent α vary from 0.7 for faults in Chimney Rock, Utah (Krantz, 1988; Cladouhos & Marrett, 1996) to 1.1 for Neogene faults in the Boso and Iura Peninsula, Japan (C. H. Scholz & Cowie, 1990) to 2.3

for faults and fractures in sandstone in Tayma, Saudi Arabia (Odling et al., 1999). Most of the previous studies used data sets consisting of 10^2-10^3 fault traces with fault lengths spanning 1-2 decades.

The magnitude of the power-law exponent determines how deformation is partitioned between small and large faults. Kautz and Sclater (1988) argued, based on laboratory experiments and observations of natural faults, that small-scale faulting is responsible for a substantial internal deformation within crustal blocks bounded by major faults. In contrast, C. H. Scholz and Cowie (1990) estimated the power-law exponent $\alpha \approx 1$ using fault trace data from Japan and argued that small faults are negligible in the total strain budget. Recently, Fialko and Jin (2021) suggested that high-angle conjugate faults ("cross-faults") in the Eastern California Shear Zone can result from a long-term relative rotation assisted by a distributed faulting. No such rotation would be possible if small faults are too scarce to accommodate a substantial fraction of tectonic strain.

To quantify the amount of deformation that can be attributed to small-scale faulting, we analyze the fault length distribution across a wide range of spatial scales using several high-quality data sets. In particular, we use detailed fault maps from different geological settings, including the Basin and Range Province (Nevada), Central Pennsylvania/Northern New Jersey, Ventura County (California), and Northern New Zealand. We complement these crustal-scale data sets with outcrop-scale observations from Eastern Israel (Bahat, 1987), Sierra Nevada (Segall & Pollard, 1983), Southern New Zealand (Davis et al., 2005), and Eastern France (Villemin et al., 1995). We also use laboratory observations of microfractures in rock samples loaded to failure at confining pressures of several tens of megapascals (Katz & Reches, 2004). We examine the compiled multi-scale data to test the assumption of a power-law distribution, obtain the best-fit power-law exponent, and use the latter to estimate the amount of strain accommodated by faults in the upper crust, as a function of fault size.

1 Data and Methods

We are interested in the fault length-frequency distribution in regions of distributed deformation such as the Eastern California Shear Zone (Dokka & Travis, 1990; Tymofyeyeva & Fialko, 2015; Fialko & Jin, 2021). Unfortunately, developing (i.e., structurally immature) strike-slip faults are often difficult to recognize due to their limited geomor-

phologic expression, especially at the low end of fault sizes. Dip-slip fault systems are better suited for this purpose. One of the most extensive and detailed fault trace data sets from an actively deforming extensional region is that from the Basin and Range (B&R) province in the Western US (Figure 1a). This region hosts a number of active Quaternary faults (e.g., Eaton, 1982; U.S. Geological Survey and Nevada Bureau of Mines and Geology, 2023). We examine fault traces from an area extending 6 degrees in longitude and 4 degrees in latitude (Figure 1a). The respective data set consists of 26512 fault traces, with the fault segment lengths varying from 2.1 m to 42.6 km.

A close inspection of the B&R fault trace data reveals that many fault traces that appear continuous on a regional scale (Figure 1a) are in fact highly segmented (Supplementary Figure S1a). While some of the apparently continuous fault traces may be segmented because they have different attributes such as dip and strike, others "may have the same attributes but are still separated at the segment level" (R. Schmitt, USGS, personal communication). To mitigate potential biases due to artificial segmentation, we developed an algorithm for concatenating individual segments that likely belong to the same fault. The algorithm attributes different segments to the same fault if the following criteria are satisfied: (1) tips of the adjacent fault segments are within a prescribed distance D from each other; (2) the adjacent fault segments are sufficiently well aligned, such that the difference in strike angles θ_1 and θ_2 between the segment tips (see Figure S2a) is less than a prescribed threshold δ; also, we require that the difference between the average of strike angles at the segment tips, $(\theta_1+\theta_2)/2$ and the strike angle of a line connecting the segment tips is less than a prescribed threshold δ (Figure S2c); (3) overlapping segments that satisfy conditions (1) and (2) are considered part of the same fault if $D < L/3$, where L is the length of a smaller segment. The latter condition is meant to avoid absorption of small faults that are sub-parallel to (rather than aligned with) the large ones. The respective criteria are illustrated in Figure S2.

A reasonable upper limit on D is some fraction of the thickness of the brittle layer T, such that the apparently discontinuous (e.g., poorly exposed) surface traces might possibly belong to the same fault at depth. For the Basin and Range province, $T \approx 15$ km (e.g., Pancha et al., 2006). We assume $D < (T/3 = 5$ km). We find that the best-fit power-law exponent is relatively insensitive to the assumed value of D, for δ between 0 and 30 degrees (Figures S3 and S4). Larger values of D and δ encourage segment linking, resulting in a smaller number of small faults, and consequently smaller absolute val-

ues of the best-fit power-law exponents. In the analysis presented below, we use $D =$ 5 km, and $\delta = 30°$ to provide a lower bound on α. A comparison of fault trace data before and after "de-segmentation" is shown in Figure S1.

Because the cumulative fault length distribution is known to be sensitive to finite size effects, which can potentially bias determination of the exponent (e.g., Bonnet et al., 2001), we use the density distribution (equation 2) to estimate the power-law exponent β, unless indicated otherwise. The respective values of α are trivially given by $\alpha = \beta - 1$.

Figure 1b shows the probability density of fault length distribution for the "concatenated" Basin and Range data set (a subset is shown in Figure S1b). To minimize the censoring bias (e.g., Torabi & Berg, 2011), we refine the data set by excluding faults that intersect the region boundaries. On a log-log plot, the density distribution exhibits a quasi-linear trend for $L > 5$ km, and flattens out for smaller L. The roll-off at $L <$ 5 km likely results from incomplete sampling (truncation bias, Torabi & Berg, 2011; Bonnet et al., 2001), analogous to saturation of the Gutenberg-Richter distribution below the magnitude of completeness (e.g., Woessner & Wiemer, 2005). The truncation bias may be due to a finite detection threshold and/or 2-D sampling of a 3-D fault population (e.g., Heifer & Bevan, 1990). We use the Kolmogorov-Smirnov (KS) test (Clauset et al., 2009) to identify the range of fault lengths $[L_{min}, L_{max}]$ that can be used for power-law fitting (see Supplementary Text S1 for details). We estimate the density power-law exponent β by the least-squares linear regression over the interval $[L_{min}, L_{max}]$. The uncertainty on the best-fit slope is obtained by performing a regression for different bin sizes, and computing a standard deviation of the resulting slope estimates. For the data shown in Figure 1, we obtain $\beta = 3.51 \pm 0.12$, or $\alpha \approx 2.5$. This can be compared to the value of $\alpha = 1.84$ estimated by Cladouhos and Marrett (1996), who used an older (presumably, less complete) fault map of the Basin and Range province, and fitted a linear trend to the cumulative fault length distribution over the fault length interval between ∼15-70 km.

We extended the same analysis to several other locations for which high-resolution maps of dip-slip faults are openly available, in particular, Central Pennsylvania and Northern New Jersey, Ventura County (California), and Northern New Zealand. Figure 2a shows fault traces from an area in Central Pennsylvania and Northern New Jersey (PA Depart-

ment of Conservation & Natural Resources, 2023; NJ Dept. of Environmental Protection Bureau of GIS, 2023). The mapped traces represent inactive thrust and strike-slip faults formed 400 to 250 million years ago (Hatcher, 1987). For consistency, we apply the same algorithm for concatenating the aligned segments as described above. The resulting data set consists of 2273 faults having length between 15 m and 108 km. The probability density fault length distribution (Figure 2b) is characterized by an apparent truncation for faults smaller than 20 km, and a slope of the quasi-linear trend of -3.51, remarkably similar to results obtained for the Basin and Range province (Figure 1b).

The Ventura County, CA (Figure 3) and Northern New Zealand (Figure 4) fault maps cover much smaller areas. After the segment concatenation procedure, each data set contains several hundreds of fault traces. This is 1-2 orders of magnitude smaller than the number of fault traces in the B&R and Pennsylvania/New Jersey data sets (Figures 1 and 2), but comparable to a typical size of data sets examined in a number of previous studies. While these smaller data sets are too characterized by decaying trends toward the high end of the sampled range of fault lengths, the data exhibit a significant scatter (e.g., Figure 4b), making power-law fits more problematic. Our analysis of the respective data sets yields smaller values of β that are subject to higher uncertainties (2.68 ± 0.14 for Ventura County and 2.42 ± 0.40 for Northern New Zealand , see Figures 3b and 4b).

To evaluate the fault length distribution at smaller scales, we use published data on fracture density measured in outcrops ($L \sim$1-100 m) and laboratory samples ($L \sim$1-100 mm). The outcrop-scale observations include joints in Eocene chalks in the Syrian Arc folding belt, Israel (Bahat, 1987); joints in igneous rocks near Florance Lake, Sierra Nevada, California (Segall & Pollard, 1983); thrust faults in the Ostler Fault Zone, Benmore outcrop, Southern New Zealand (Davis et al., 2005); and predominantly dip-slip faults in La Houve Coal Field, an old sedimentary basin in Eastern France that experienced both compressional and extensional tectonics (Villemin et al., 1995). The laboratory data are from specimens of Mount Scott granite of Oklahoma loaded to peak yield stress in a triaxial apparatus under confining pressure of 41 MPa (Katz & Reches, 2004). The micro-structural mapping of the sample damage was performed on scanned images of thin sections. Each sample had on the order of 10^3 resolved micro-fractures with lengths between 0.01-10 mm (Katz & Reches, 2004).

A compilation of the respective data sets is presented in Figure 5, along with the fault trace data from Figures 1-4. To enable a direct comparison of different data sets, we normalize the cumulative fault length counts by the areas from which the fault trace data were collected. The combined cumulative frequency distribution spans 8 decades of fault length, and 18 decades of fault density (cumulative fault counts per unit area). All of the individual data sets shown in Figure 5 appear to have a log-normal distribution, with a quasi-linear trend at the high end, and a roll-off at the low end of the respective fault lengths. However, the combined data set admits a common envelope, with a slope that closely matches those of most of individual data sets. The least squares fit of the common envelope (see solid black line in Figure 5) yields a power-law exponent of $\alpha \approx 2.16$.

2 Strain due to faults obeying a power law distribution

An overall agreement of the estimated power-law exponents of individual data sets between each other, on the one hand, and the common envelope, on the other hand (Figure 5), lends support to a suggestion that the roll off in individual data sets is a result of truncation (e.g., due to a detection threshold, Bonnet et al., 2001; Torabi & Berg, 2011), and that the fault length statistics is adequately described by a power law across a wide range of spatial scales. If so, one can evaluate the amount of tectonic strain absorbed by faults of different sizes (e.g., C. H. Scholz & Cowie, 1990; J. Walsh et al., 1991).

For a population of n faults within the brittle crust having a volume TA, where T is the thickness of the brittle layer, and A is the map area, the average strain accommodated by faulting is given by (Kostrov, 1974):

$$\varepsilon_{ij} = \frac{1}{2TA} \sum_{k=1}^{n} {}^{k}P_{ij}. \tag{3}$$

In equation (3), ${}^{k}P_{ij}$ is the seismic potency tensor (e.g., Ben-Zion, 2001) of the k-th fault in a population. The average fault slip S is expected to scale with fault length L,

$$S \propto L^{m}. \tag{4}$$

Theoretical arguments and field observations suggest that m should be close to 1 (e.g., Cowie & Scholz, 1992; Fialko, 2015), although higher values of m were suggested as well (e.g., J. J. Walsh & Watterson, 1988; Marrett & Allmendinger, 1991). Assuming $m =$

1,

$$S = \epsilon L, \tag{5}$$

where ϵ is the critical shear strain drop corresponding to fault propagation. The scalar potency is $P = \gamma S L^2$ for faults smaller than T, and $P = \gamma S L T$ otherwise, where γ is a geometric factor of the order of unity that accounts for the fault shape and fault dip (for faults that cut through the entire brittle layer, e.g., Vavra et al., 2023). For simplicity, hereafter we assume $\gamma = 1$. The number of faults within an interval of fault lengths ΔL is $(dN(L)/dL)\Delta L$. The cumulative potency can be calculated by integrating potencies of all faults for a given range of fault lengths. For faults smaller than T, the cumulative potency is (C. H. Scholz & Cowie, 1990):

$$p_1(L_{min}, L_{max}) = \sum_k {}^k P = -\epsilon \int_{L_{min}}^{L_{max}} \frac{dN(L)}{dL} L^3 dL = C\epsilon \frac{\alpha}{3-\alpha} L^{3-\alpha} \Big|_{L_{min}}^{L_{max}}, \tag{6}$$

where L_{min} and L_{max} are the minimum and maximum fault sizes, respectively. For faults that cut through the entire brittle layer ($L > T$),

$$p_2(L_{min}, L_{max}) = \sum_k {}^k P = -\epsilon T \int_{L_{min}}^{L_{max}} \frac{dN(L)}{dL} L^2 dL = C\epsilon T \frac{\alpha}{2-\alpha} L^{2-\alpha} \Big|_{L_{min}}^{L_{max}}. \tag{7}$$

We evaluate the relative contribution of faults smaller than a given size L to the total strain by allowing $L_{min} \to 0$, and computing a ratio

$$R = 100\% \times \begin{cases} \frac{p_1(0,L)}{p_1(0,T)+p_2(T,L_{max})}, & \text{for } L < T \\ \frac{p_1(0,T)+p_2(T,L)}{p_1(0,T)+p_2(T,L_{max})}, & \text{for } L > T. \end{cases} \tag{8}$$

Note that R does not depend on factors C and ϵ. Figure 6 shows the percentage of strain accommodated by faults having length less than L, for a range of L, assuming $\alpha = 2.16$, $L_{max} = 100$ km (Figure 5), and $T = 15$ km, typical of the seismogenic depth in many tectonically active areas (e.g., Pancha et al., 2006; E. O. Lindsey & Fialko, 2016; Jin et al., 2023; Jia et al., 2023). For a comparison, we also show analogous calculations for previously reported values of $\alpha = 1.1$ (dashed line, C. H. Scholz & Cowie, 1990) and $\alpha = 2.34$ (dotted line, Odling et al., 1999).

3 Discussion

For fault systems characterized by a power-law size distribution (1), the power-law exponent α controls how much of tectonic deformation is accommodated by numerous small faults versus a few large ones. C. H. Scholz and Cowie (1990) estimated the value

of $\alpha = 1.1$ for a set of intraplate faults in Japan, and concluded that small faults are negligible in the overall strain budget. This is because integrals (6) and (7) are strongly convergent for $\alpha \approx 1$, so that the cumulative potency is dominated by the largest faults. Our results, based on a much larger data set, indicate $\alpha \geq 2$ (Figure 5). Most of the previously published estimates of α fall in the range between 1 and 2 (e.g., Bonnet et al., 2001). Possible reasons for different values of α reported in the literature include: (i) use of fault trace data of limited coverage and/or resolution; (ii) uncertainties involved in defining fault connectivity; (iii) a narrow range of fault lengths used in the analysis; (iv) departures from self-similarity due to the presence of intrinsic length scales; (v) different stages of maturity of different fault systems. For example, the data set used by C. H. Scholz and Cowie (1990) spans only one order of magnitude of fault lengths, from ∼10 to ∼100 km, likely insufficient for a robust validation of a power-law distribution (Stumpf & Porter, 2012). C. Scholz et al. (1993) analyzed a data set from the Volcanic Tableland (California) with fault lengths spanning 2 orders of magnitude, from a few tens of meters to a few kilometers, and obtained a higher value of $\alpha \approx 1.3$. The latter underpredicts the slope at the upper tail of the fault length distribution of C. Scholz et al. (1993, their figure 4), which the authors attributed to data censoring.

Our analysis of several high-resolution data sets (Figures 1-5) suggests values of α close to 2, higher than those reported by C. H. Scholz and Cowie (1990) and C. Scholz et al. (1993), but consistent with results from other multi-resolution studies. In particular, Heifer and Bevan (1990) combined fault trace data with measurements of crack density in boreholes to infer $\alpha \approx 2$. Odling et al. (1999) performed a multi-scale analysis of the length distribution of faults in sandstones in Saudi Arabia, and found the best-fit power-law exponent of 2.34 for a range of fault lengths spanning 4 orders of magnitude. C. Scholz et al. (1993) cautioned against combining observations that include different fracture modes (e.g., faults and joints, Heifer & Bevan, 1990). However, it can be argued that the crack length distributions should not strongly depend on the fracture mode as mathematical expressions for stress fields due to shear and tensile cracks are essentially identical (e.g., Fialko, 2015), so that stress interactions within the crack network are expected to be similar (e.g., for shear and tensile cracks). An overall agreement between the estimated power-law exponents for different types of fractures, as well as for data sets from different locations (Figure 5) lends support to a hypothesis that

faulting is governed by a "universal" power law with $\alpha \approx 2$ (King, 1983; Proekt et al., 2012; Roman & Bertolotti, 2022), at least at the initial stages of failure.

We point out that the data set used by C. H. Scholz and Cowie (1990) is dominated by "long" ($L > T$) faults that accumulated a substantial amount of slip, and thus might be more representative of a structurally mature fault system. Experimental studies indeed reveal higher values of α at the initial stages of faulting when deformation is broadly distributed, and a decrease to $\alpha \approx 1$ with an increasing system maturity (e.g., Sornette et al., 1993; Hatton et al., 1993; Cladouhos & Marrett, 1996). It follows that small faults can potentially accommodate a substantial fraction of tectonic strain at the initial stages of faulting (e.g., in developing shear zones). Over time, as faults grow and connect, deformation may localize to major faults that eventually take up most of the deformation.

These arguments suggest an important distinction between deformation styles due to immature shear zones such as the Eastern California Shear Zone (Dokka & Travis, 1990; Floyd et al., 2020), and mature well-slipped plate boundary faults such as the San Andreas Fault (Lisowski et al., 1991; Fialko, 2006). In the latter case, interseismic strain accumulation is equal in magnitude, but opposite in sign to strain released in large earthquakes, so the patterns of interseismic and long-term (geologic) displacements across a mature fault are very different (Figure 7). A complete or nearly complete recovery of interseismic strain (i.e., elastic rebound) is evidenced by good agreement between "geologic" and "geodetic" slip rates on major plate boundary faults (e.g., Schmalzle et al., 2006; Tatar et al., 2012; E. Lindsey & Fialko, 2013). In contrast, immature fault systems with $\alpha \geq 2$ give rise to a distributed inelastic deformation with the long-term displacement profile that may closely mimic the observed interseismic velocities (Fialko & Jin, 2021). The diffuse deformation pattern illustrated in Figure 7a can be thought of as resulting from the "seismic flow of rocks", as originally envisioned by Riznichenko (1965) and Kostrov (1974), although a more appropriate term would be the "brittle flow of rocks", since some of the deformation may occur aseismically, e.g. via creep (Tymofyeyeva et al., 2019; Kaneko et al., 2013) or the bulk yielding (Donath & Parker, 1964; Hamiel et al., 2006).

The relative contribution of small faults to the strain budget is expected to be larger for smaller values of L_{max}, and/or larger values of α. We note that the estimated values of α may in fact be lower bounds due to two-dimensional (2-D) sampling of three-

dimensional (3-D) fault populations. For example, for uniformly distributed and randomly oriented faults, the true (i.e., 3-D) exponent is predicted to be larger than the exponent inferred from the 2-D sampling by as much as 1 unit (e.g., Bonnet et al., 2001; Marrett & Allmendinger, 1991). This only applies to small ($L < D$) faults, as for large faults the distribution is essentially 2-D. For α approaching 3, small faults would actually dominate the strain budget, and the contribution of large faults would be negligible. Note that for the cumulative potency and strain to remain finite, α cannot exceed 3 (eq. 6).

Taking at face value the estimated power law-exponent $\alpha \approx 2$ (Figure 5), we find that small ($L < T$) faults may take up more than one third of the total strain, which is almost an order of magnitude greater than predicted for $\alpha \approx 1$ (Figure 6). A power law-exponent $\alpha \geq 2$ may provide an explanation for the "missing strain" in palinspastic restorations of faults in sedimentary basins, as well as in laboratory models of tectonic extension using analog materials (e.g., Kautz & Sclater, 1988; Marrett & Allmendinger, 1992; J. Walsh et al., 1991). The bulk inelastic deformation accommodated by small faults can result in rotation of faults away from the optimal orientation, and increases in dihedral angles between conjugate faults, as often observed in active shear zones (e.g., Ron et al., 2001; Fialko, 2021; Zou et al., 2023). It might also account for the reported differences between geologic and geodetic slip rates in regions of diffuse deformation. In particular, models of deformation across the plate boundary in California suggest that up to 30% of deformation is accommodated off of the known faults (Field et al., 2014). Similar conclusions are drawn from numerical models of continental extension (Pan et al., 2023). Given no resolvable difference between the geologic and geodetic slip rates of mature high-slip-rate faults such as the San Andreas and San Jacinto faults (Segall, 2002; E. O. Lindsey et al., 2014; Tymofyeyeva & Fialko, 2018; Schmalzle et al., 2006), most of the "missing slip" is apparently associated with regions of diffuse deformation characterized by low strain rates such as the Eastern California Shear Zone (Herbert et al., 2014). The same may apply to other areas of broadly distributed continental deformation such as the India-Eurasia collision zone (e.g., Garthwaite et al., 2013; Wang & Shen, 2020). Finally, we note that the non-negligible contributions of small faults to finite strain suggested by our analysis contrasts with the seismic moment release which is strongly dominated by largest events (e.g., Bell et al., 2013). This is likely due to the fact that only a fraction of faults that exist within the seismogenic zone are seismically active at any given time. One mechanism for eventual de-activation of pre-existing or newly formed

faults is rotation of fault planes away from the principal compression axis with increasing finite strain (e.g., Ron et al., 2001; Fialko & Jin, 2021; Zou et al., 2023).

4 Conclusions

We analyzed the fault length frequency distribution using high-resolution fault trace data from diverse settings including Basin and Range Province, Central Pennsylvania/Northern New Jersey, Ventura County, California, and Northern New Zealand. To extend our analysis to smaller scales, we included published outcrop data from Sierra Nevada, Eastern Israel, Southern New Zealand, and Eastern France, and laboratory data from experiments on the initially intact granite samples. Our results indicate that while each individual data set yields an apparent log-normal distribution of fault lengths, a composite multi-scale data set reveals a fault length-distribution that follows a power law over 8 decades of fault lengths, with a cumulative power-law exponent $\alpha \approx 2$. The obtained best-fit value may be an under-estimate of the true value of the power-law exponent given an observation bias (2-D sampling of 3-D faults). We used the best-fit value of the power-law exponent to estimate a fraction of strain accommodated by faults as a function of fault size. We find that small faults ($L < 15$ km) can accommodate a substantial (up to 40%) fraction of tectonic strain, at least at the initial stages of faulting. A continued deformation may give rise to a transition from self-similar fault networks to highly localized mature faults.

Acknowledgments

We thank reviewers... This study was supported by NSF (EAR-1841273) and NASA (80NSSC22K0506). Figures were produced using Generic Mapping Tools (GMT) (Wessel et al., 2013) and Matlab. The authors declare no competing interests.

Data Availability Statement

The fault trace data used in this paper are available at `10.5281/zenodo.10938802`.

References

Bahat, D. (1987). Jointing and fracture interactions in Middle Eocene chalks near Beer Sheva, Israel. *Tectonophysics*, *136*(3), 299-321.

Bell, A. F., Naylor, M., & Main, I. G. (2013). Convergence of the frequency-size dis-

tribution of global earthquakes. *Geophys. Res. Lett.*, *40*(11), 2585–2589.

Bense, V., Gleeson, T., Loveless, S., Bour, O., & Scibek, J. (2013). Fault zone hydrogeology. *Earth-science reviews*, *127*, 171-192.

Ben-Zion, Y. (2001). On quantification of the earthquake source. *Seismol. Res. Lett.*, *72*(2), 151–152.

Ben-Zion, Y., & Sammis, C. G. (2003). Characterization of fault zones. *Pure Appl. Geophys.*, *160*(3), 677–715.

Bonnet, E., Bour, O., Odling, N. E., Davy, P., Main, I., Cowie, P., & Berkowitz, B. (2001). Scaling of fracture systems in geological media. *Reviews of Geophysics*, *39*(3), 347-383.

Bour, O., & Davy, P. (1999). Clustering and size distributions of fault patterns: Theory and measurements. *Geophys. Res. Lett.*, *26*(13), 2001-2004.

Bürgmann, R., & Pollard, D. D. (1994). Strain accommodation about strike-slip fault discontinuities in granitic rock under brittle-to-ductile conditions. *J. Struct. Geol.*, *16*(12), 1655-1674.

Childs, C., Walsh, J. J., & Watterson, J. (1990). A method for estimation of the density of fault displacements below the limits of seismic resolution in reservoir formations. In *North sea oil and gas reservoirs—ii* (p. 309-318). Springer Netherlands.

Cladouhos, T. T., & Marrett, R. (1996). Are fault growth and linkage models consistent with power-law distributions of fault lengths? *J. Struct. Geol.*, *18*, 281–293.

Clark, R. M., Cox, S., & Laslett, G. M. (1999). Generalizations of power-law distributions applicable to sampled fault-trace lengths: model choice, parameter estimation and caveats. *Geophys. J. Int.*, *136*(2), 357–372.

Clauset, A., Shalizi, C. R., & Newman, M. E. J. (2009). Power-law distributions in empirical data. *SIAM Review*, *51*(4), 661-703.

Cowie, P. A., & Scholz, C. H. (1992). Physical explanation for the displacement-length relationship of faults using a post-yield fracture mechanics model. *J. Struct. Geol.*, *14*, 1133–1148.

Cox, R. T., Van Arsdale, R. B., Harris, J. B., & Larsen, D. (2001). Neotectonics of the southeastern Reelfoot rift zone margin, central United States, and implications for regional strain accommodation. *Geology*, *29*(5), 419-422.

Cox, S., & Scholz, C. (1988). On the formation and growth of faults: an experimental study. *J. Struct. Geol.*, *10*(4), 413-430.

Davis, K., Burbank, D. W., Fisher, D., Wallace, S., & Nobes, D. (2005). Thrust-fault growth and segment linkage in the active Ostler fault zone, New Zealand. *J. Struct. Geol.*, *27*(8), 1528-1546.

Dawers, N. H., & Anders, M. H. (1995). Displacement-length scaling and fault linkage. *J. Struct. Geol.*, *17*(5), 607-614.

Dokka, R. K., & Travis, C. J. (1990). Role of the Eastern California shear zone in accommodating Pacific-North American plate motion. *Geophys. Res. Lett.*, *17*, 1323–1327.

Donath, F. A., & Parker, R. B. (1964). Folds and folding. *Geol. Soc. Am. Bull.*, *75*, 45–62.

Eaton, G. P. (1982). The Basin and Range province: origin and tectonic significance. *Ann. Rev. Earth Planet. Sci.*, *10*(1), 409-440.

Fialko, Y. (2006). Interseismic strain accumulation and the earthquake potential on the southern San Andreas fault system. *Nature*, *441*, 968–971.

Fialko, Y. (2015). Fracture and Frictional Mechanics - Theory. In G. Schubert (Ed.), *Treatise on geophysics, 2nd. ed., vol. 4* (pp. 73–91). Elsevier Ltd., Oxford.

Fialko, Y. (2021). Estimation of absolute stress in the hypocentral region of the 2019 Ridgecrest, California, earthquakes. *J. Geophys. Res.*, *126*, e2021JB022000.

Fialko, Y., & Jin, Z. (2021). Simple shear origin of the cross-faults ruptured in the 2019 Ridgecrest earthquake sequence. *Nat. Geosci.*, *14*, 513–518.

Field, E. H., Arrowsmith, R. J., Biasi, G. P., Bird, P., Dawson, T. E., Felzer, K. R., ... others (2014). Uniform California Earthquake Rupture Forecast, version 3 (UCERF3) The time-independent model. *Bull. Seism. Soc. Am.*, *104*, 1122–1180.

Floyd, M., Funning, G., Fialko, Y. A., Terry, R. L., & Herring, T. (2020). Survey and Continuous GNSS in the vicinity of the July 2019 Ridgecrest earthquakes. *Seismol. Res. Lett.*, *91*, 2047–2054.

Fossen, H. (2020). Chapter 8 - fault classification, fault growth and displacement. In N. Scarselli, J. Adam, D. Chiarella, D. G. Roberts, & A. W. Bally (Eds.), *Regional geology and tectonics (second edition)* (p. 119-147). Elsevier.

Garthwaite, M. C., Wang, H., & Wright, T. J. (2013). Broadscale interseismic de-

formation and fault slip rates in the central Tibetan Plateau observed using InSAR. *J. Geophys. Res.*, *118*(9), 5071–5083.

Gupta, A., & Scholz, C. H. (2000). Brittle strain regime transition in the Afar depression: Implications for fault growth and seafloor spreading. *Geology*, *28*(12), 1087-1090.

Hamiel, Y., Katz, O., Lyakhovsky, V., Reches, Z., & Fialko, Y. (2006). Stable and unstable damage growth in rocks with implications to fracturing of granite. *Geophys. J. Int.*, *167*, 1005–1016.

Hatcher, R. D. (1987). Tectonics of the Southern and Central Appalachian Internides. *Ann. Rev. Earth Planet. Sci.*, *15*(1), 337-362.

Hatton, C., Main, I., & Meredith, P. (1993). A comparison of seismic and structural measurements of scaling exponents during tensile subcritical crack growth. *J. Struct. Geol.*, *15*, 1485–1495.

Heifer, K., & Bevan, T. (1990). Scaling relationships in natural fractures-data, theory and applications. In *Proc. eur. petrol. conf.* (Vol. 2, pp. 367–376).

Herbert, J. W., Cooke, M. L., Oskin, M., & Difo, O. (2014). How much can off-fault deformation contribute to the slip rate discrepancy within the eastern California shear zone? *Geology*, *42*, 71–75.

Jia, Z., Jin, Z., Marchandon, M., Ulrich, T., Gabriel, A.-A., Fan, W., ... others (2023). The complex dynamics of the 2023 Kahramanmaraş, Turkey, M w 7.8-7.7 earthquake doublet. *Science*, *381*(6661), 985–990.

Jin, Z., Fialko, Y., Yang, H., & Li, Y. (2023). Transient deformation excited by the 2021 M7.4 Maduo (China) earthquake: Evidence of a deep shear zone. *J. Geophys. Res.*, *128*, e2023JB026643.

Kaneko, Y., Fialko, Y., Sandwell, D., Tong, X., & Furuya, M. (2013). Interseismic deformation and creep along the central section of the North Anatolian Fault (Turkey): InSAR observations and implications for rate-and-state friction properties. *J. Geophys. Res.*, *118*(1), 316–331.

Katz, O., & Reches, Z. (2004). Microfracturing, damage, and failure of brittle granites. *Journal of Geophysical Research: Solid Earth*, *109*(B1).

Kautz, S. A., & Sclater, J. G. (1988). Internal deformation in clay models of extension by block faulting. *Tectonics*, *7*(4), 823-832.

King, G. C. P. (1983). The accomodation of large strains in the upper lithosphere of

the earth and other solids by self-similar fault systems: the geometric origin of b-value. *Pure Appl. Geophys.*, *121*, 761–815.

Kostrov, B. V. (1974). Seismic moment and energy of earthquakes and seismic flow of rock. *Izv., Acad. Sci., USSR, Phys. Solid Earth (Engl. Translation)*, *1*, 23–40.

Krantz, R. W. (1988). Multiple fault sets and three-dimensional strain: Theory and application. *J. Struct. Geol.*, *10*(3), 225-237.

Lindsey, E., & Fialko, Y. (2013). Geodetic slip rates in the Southern San Andreas Fault System: Effects of elastic heterogeneity and fault geometry. *J. Geophys. Res.*, *118*, 689–697.

Lindsey, E. O., & Fialko, Y. (2016). Geodetic constraints on frictional properties and earthquake hazard in the Imperial Valley, Southern California. *J. Geophys. Res.*, *121*, 1097–1113.

Lindsey, E. O., Sahakian, V. J., Fialko, Y., Bock, Y., Barbot, S., & Rockwell, T. K. (2014). Interseismic strain localization in the San Jacinto fault zone. *Pure and Applied Geophysics*, *171*(11), 2937–2954.

Lisowski, M., Savage, J., & Prescott, W. H. (1991). The velocity field along the San Andreas fault in central and southern California. *J. Geophys. Res.*, *96*, 8369–8389.

Louderback, G. D. G. D. (1950). *Faults and engineering geology.* United States: Geological Society of America.

Mansfield, C., & Cartwright, J. (2001). Fault growth by linkage: observations and implications from analogue models. *J. Struct. Geol.*, *23*(5), 745-763.

Marrett, R., & Allmendinger, R. W. (1991). Estimates of strain due to brittle faulting: sampling of fault populations. *J. Struct. Geol.*, *13*, 735–738.

Marrett, R., & Allmendinger, R. W. (1992). Amount of extension on "small" faults: An example from the Viking graben. *Geology*, *20*, 47–50.

Nicol, A., Walsh, J., Watterson, J., & Gillespie, P. (1996). Fault size distributions — are they really power-law? *J. Struct. Geol.*, *18*(2), 191-197.

NJ Dept. of Environmental Protection Bureau of GIS. (2023). *Geologic faults in New Jersey.*

Odling, N., Gillespie, P., Bourgine, B., Castaing, C., Chiles, J., Christensen, N., ... others (1999). Variations in fracture system geometry and their implications

for fluid flow in fractures hydrocarbon reservoirs. *Petroleum Geoscience*, *5*, 373–384.

Ojo, O. O., Ohenhen, L. O., Kolawole, F., Johnson, S. G., Chindandali, P. R., Atekwana, E. A., & Lao-Davila, D. A. (2022). Under-displaced normal faults: Strain accommodation along an early-stage rift-bounding fault in the Southern Malawi Rift. *Frontiers in earth science*, *10*.

PA Department of Conservation & Natural Resources. (2023). *Bedrock geology of Pennsylvania - faults (vector).*

Pan, S., Naliboff, J., Bell, R., & Jackson, C. (2023). How do rift-related fault network distributions evolve? quantitative comparisons between natural fault observations and 3D numerical models of continental extension. *Tectonics*, *42*(10), e2022TC007659.

Pancha, A., Anderson, J. G., & Kreemer, C. (2006). Comparison of seismic and geodetic scalar moment rates across the Basin and Range Province. *Bull. Seism. Soc. Am.*, *96*, 11–32.

Proekt, A., Banavar, J. R., Maritan, A., & Pfaff, D. W. (2012). Scale invariance in the dynamics of spontaneous behavior. *Proc. Natl. Acad. Sci.*, *109*, 10564–10569.

Riznichenko, Y. V. (1965). The flow of rocks as related to seismicity. *Dokl. Akad. Nauk SSSR*, *161*(1), 96–98.

Roman, S., & Bertolotti, F. (2022). A master equation for power laws. *Royal Society Open Science*, *9*(12), 220531.

Ron, H., Beroza, G., & Nur, A. (2001). Simple model explains complex faulting. *Eos, Transactions American Geophysical Union*, *82*(10), 125–129.

Rotevatn, A., Jackson, C. A.-L., Tvedt, A. B., Bell, R. E., & Blækkan, I. (2019). How do normal faults grow? *J. Struct. Geol.*, *125*, 174–184.

Rui, X., & Stamps, D. S. (2019). Strain accommodation in the Daliangshan mountain area, southeastern margin of the Tibetan Plateau. *J. Geophys. Res. Solid Earth*, *124*(9), 9816-9832.

Schmalzle, G., Dixon, T., Malservisi, R., & Govers, R. (2006). Strain accumulation across the Carrizo segment of the San Andreas Fault, California: Impact of laterally varying crustal properties. *J. Geophys. Res.*, *111*, B05403.

Scholz, C., Dawers, N., Yu, J.-Z., Anders, M., & Cowie, P. (1993). Fault growth and

fault scaling laws: Preliminary results. *J. Geophys. Res.*, *98*, 21951–21961.

Scholz, C. H., & Cowie, P. A. (1990). Determination of total strain from faulting using slip measurements. *Nature*, *346*(6287), 837-839.

Segall, P. (2002). Integrating geologic and geodetic estimates of slip rate on the San Andreas fault system. *Int. Geol. Rev.*, *44*, 62–82.

Segall, P., & Pollard, D. D. (1983). Joint formation in granitic rock of the Sierra Nevada. *GSA Bulletin*, *94*(5), 563-575.

Sornette, A., Davy, P., & Sornette, D. (1993). Fault growth in brittle-ductile experiments and the mechanics of continental collisions. *J. Geophys. Res.*, *98*, 12111–12139.

Stumpf, M. P., & Porter, M. A. (2012). Critical truths about power laws. *Science*, *335*, 665–666.

Tatar, O., Poyraz, F., Gürsoy, H., Cakir, Z., Ergintav, S., Akpınar, Z., ... others (2012). Crustal deformation and kinematics of the Eastern Part of the North Anatolian Fault Zone (Turkey) from GPS measurements. *Tectonophysics*, *518*, 55–62.

Torabi, A., & Berg, S. S. (2011). Scaling of fault attributes: A review. *Marine and Petroleum Geology*, *28*(8), 1444-1460.

Turcotte, D. (1986). A fractal model for crustal deformation. *Tectonophysics*, *132*(1), 261-269.

Tymofyeyeva, E., & Fialko, Y. (2015). Mitigation of atmospheric phase delays in InSAR data, with application to the Eastern California Shear Zone. *J. Geophys. Res.*, *120*, 5952–5963.

Tymofyeyeva, E., & Fialko, Y. (2018). Geodetic evidence for a blind fault segment at the Southern end of the San Jacinto Fault Zone. *J. Geophys. Res.*, *123*, 878–891.

Tymofyeyeva, E., Fialko, Y., Jiang, J., Xu, X., Sandwell, D., Bilham, R., ... Moafipoor, S. (2019). Slow slip event on the southern San Andreas fault triggered by the 2017 M_w8.2 Chiapas (Mexico) earthquake. *J. Geophys. Res.*, *124*, 9956–9975.

U.S. Geological Survey and Nevada Bureau of Mines and Geology. (2023). *Quaternary fault and fold database for the united states, accessed mar 1.*

Vavra, E. J., Qiu, H., Chi, B., Share, P.-E., Allam, A., Morzfeld, M., ... Fialko, Y.

(2023). Active dipping interface of the Southern San Andreas fault revealed by space geodetic and seismic imaging. *J. Geophys. Res.*, *128*, e2023JB026811.

Villemin, T., Angelier, J., & Sunwoo, C. (1995). Fractal distribution of fault length and offsets: Implications of brittle deformation evaluation—The Lorraine coal basin. In C. C. Barton & P. R. La Pointe (Eds.), *Fractals in the earth sciences* (pp. 205–226). Boston, MA: Springer US.

Walsh, J., Watterson, J., & Yielding, G. (1991). The importance of small-scale faulting in regional extension. *Nature*, *351*, 391–393.

Walsh, J. J., & Watterson, J. (1988). Analysis of the relationship between displacements and dimensions of faults. *J. Struct. Geol.*, *10*, 239–247.

Wang, M., & Shen, Z.-K. (2020). Present-day crustal deformation of continental China derived from GPS and its tectonic implications. *J. Geophys. Res.*, *125*(2), e2019JB018774.

Wessel, P., Smith, W. H. F., Scharroo, R., Luis, J., & Wobbe, F. (2013). Generic Mapping Tools: Improved Version Released. *Eos, Trans. AGU*, *94*, 409–410.

Woessner, J., & Wiemer, S. (2005). Assessing the quality of earthquake catalogues: Estimating the magnitude of completeness and its uncertainty. *Bull. Seism. Soc. Am.*, *95*(2), 684–698.

Zou, X., Fialko, Y., Dennehy, A., Cloninger, A., & Semnani, S. J. (2023). High-angle active conjugate faults in the Anza-Borrego Shear Zone, Southern California. *Geophys. Res. Lett.*, *50*, e2023GL105783.

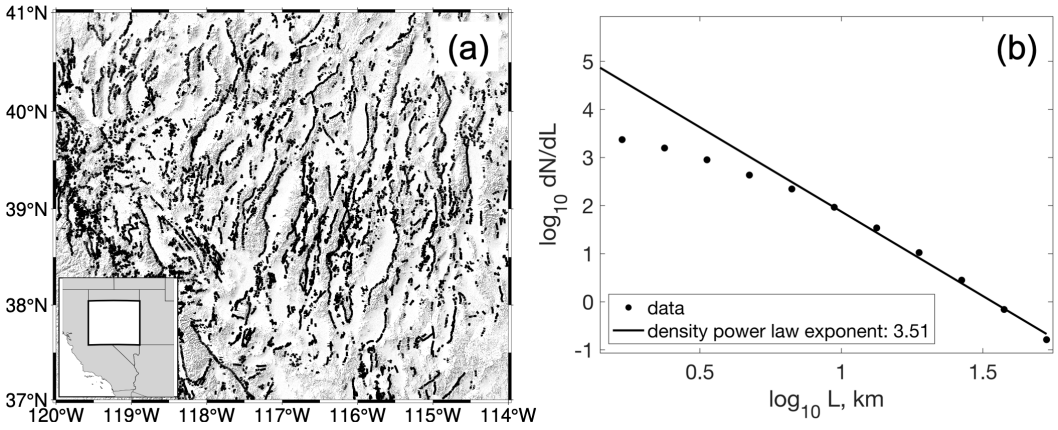

Figure 1. (a) Map of the Basin and Range Province. Shading denotes topography. Black lines denote fault traces. Inset shows location of the area of interest (white rectangle) in a regional context; thin black lines indicate state boundaries. The concatenated fault data set includes 10825 fault segments. The minimum segment length is 2.1 m and the maximum length is 49 km. (b): Probability density of the fault length distribution, on a log-log scale. Solid line represents the best linear fit at the high end of the fault length distribution ($L > 5$ km). The estimated power-law exponent (slope of the best-fit line) is $\beta = 3.51 \pm 0.12$.

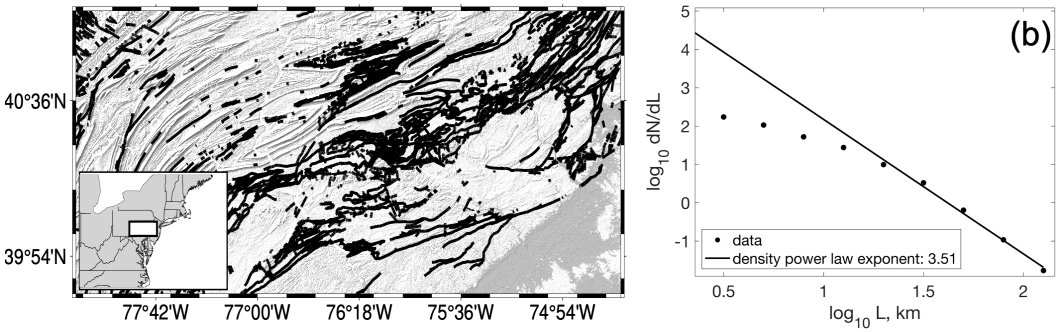

Figure 2. (a) Map of Central Pennsylvania and Northern New Jersey. Notation is the same as in Figure 1. The concatenated fault data set includes 2273 fault segments. The minimum segment length is 15 m and the maximum length is 108 km. (b) Probability density of the fault length distribution, on a log-log scale. Solid line represents the best linear fit at the high end of the fault length distribution ($L > 10$ km). The estimated power-law exponent (slope of the best-fit line) is $\beta = 3.51 \pm 0.20$.

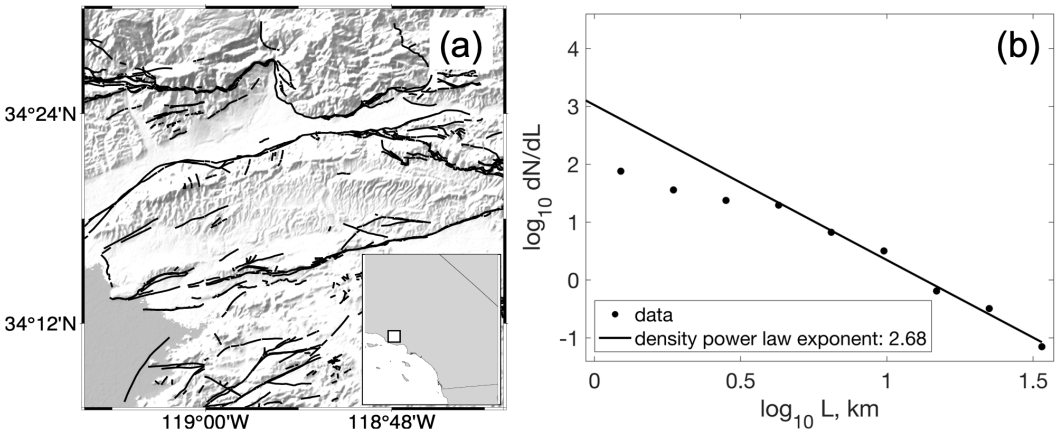

Figure 3. (a) Map of Ventura County, CA. Notation is the same as in Figure 1. The concatenated fault data set includes 349 fault segments. The minimum segment length is 0.6 m and the maximum length is 30 km. (b) Probability density of the fault length distribution, on a log-log scale. Solid line represents the best linear fit at the high end of the fault length distribution ($L > 3$ km). The estimated power-law exponent (slope of the best-fit line) is $\beta = 2.68 \pm 0.14$.

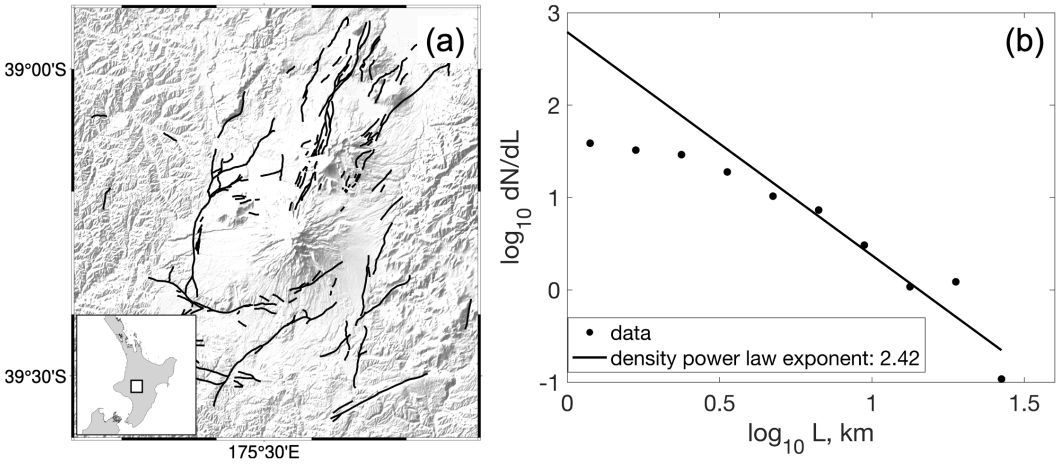

Figure 4. (a) Map of Northern New Zealand. Notation is the same as in Figure 1. The concatenated fault data set includes 159 fault segments. The minimum segment length is 363 m and the maximum length is 24.7 km. (b) Probability density of the fault length distribution, on a log-log scale. The solid line represents the best linear fit at the high end of the fault length distribution ($L > 4$ km). The estimated power-law exponent (slope of the best-fit line) is $\beta = 2.42 \pm 0.35$.

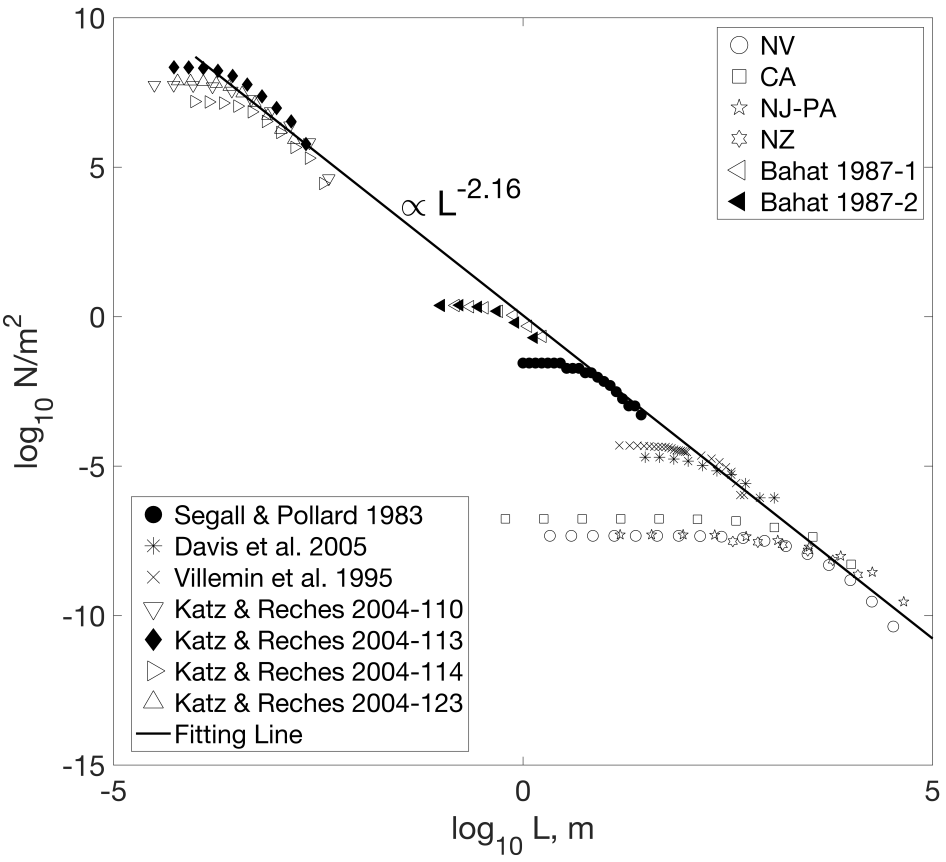

Figure 5. Cumulative fault length frequency distribution for a combined data set including fault traces (Figures 1-4), as well as outcrop-scale and lab data, normalized by the respective observation areas, on a log-log scale. The solid line is the least-squares fit for the "high-end" asymptotes of all constituent data sets. The estimated power-law exponent is $\alpha = 2.16$.

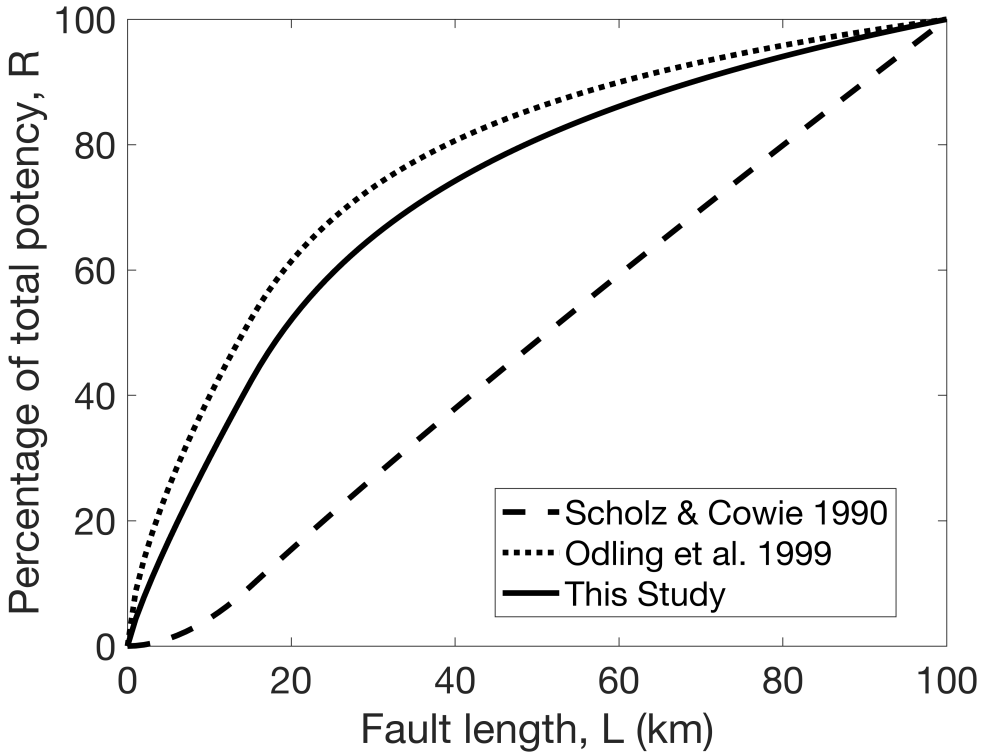

Figure 6. Percentage of the total potency R (equation 8) accommodated by faults having length less than L, for several estimated values of the power-law exponent α: solid line, $\alpha = 2.16$ (this study); dotted line, $\alpha = 2.34$ (Odling et al., 1999); dashed line, $\alpha = 1.1$ (C. H. Scholz & Cowie, 1990). We assume $L_{max} = 100$ km (Figure 5).

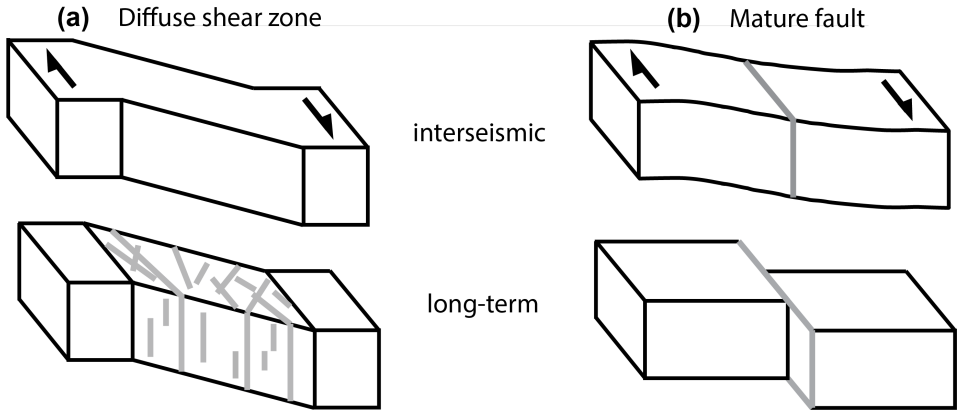

Figure 7. Schematic representation of kinematics of (a) developing shear zone and (b) mature plate boundary fault. Top and bottom panels denote interseismic and long-term (averaged over multiple earthquake cycles) motion, respectively. Gray lines denote active faults.

Figure 1.

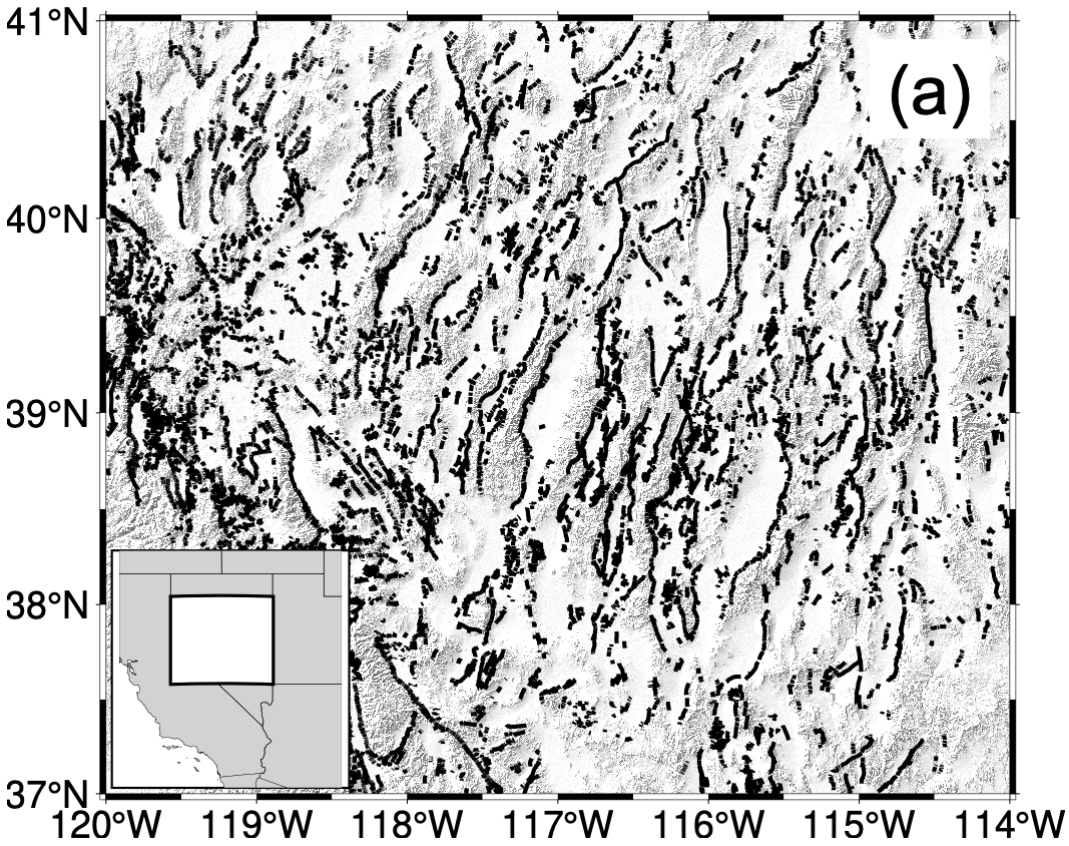
(a)
41°N
40°N
39°N
38°N
37°N
120°W
119°W
118°W
117°W
116°W
115°W
114°W

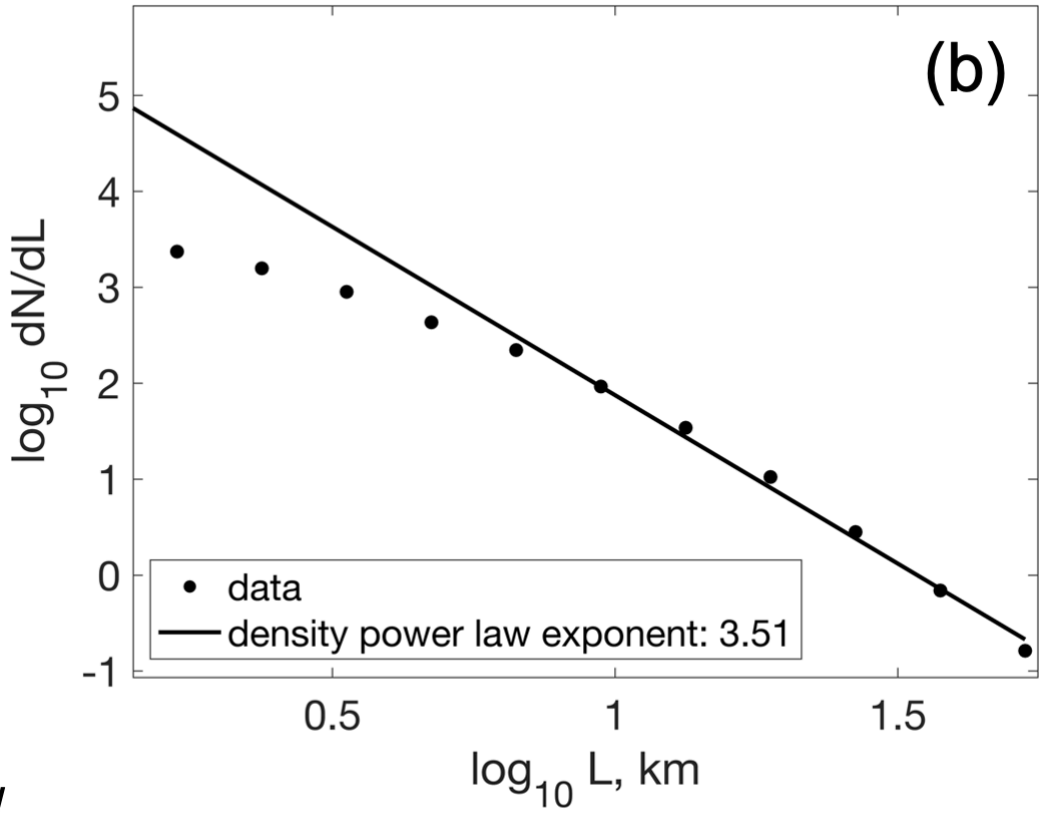
(b)
log10 dN/dL
log10 L, km
data
density power law exponent: 3.51
5
4
3
2
1
0
-1
0.5
1
1.5

Figure 2.

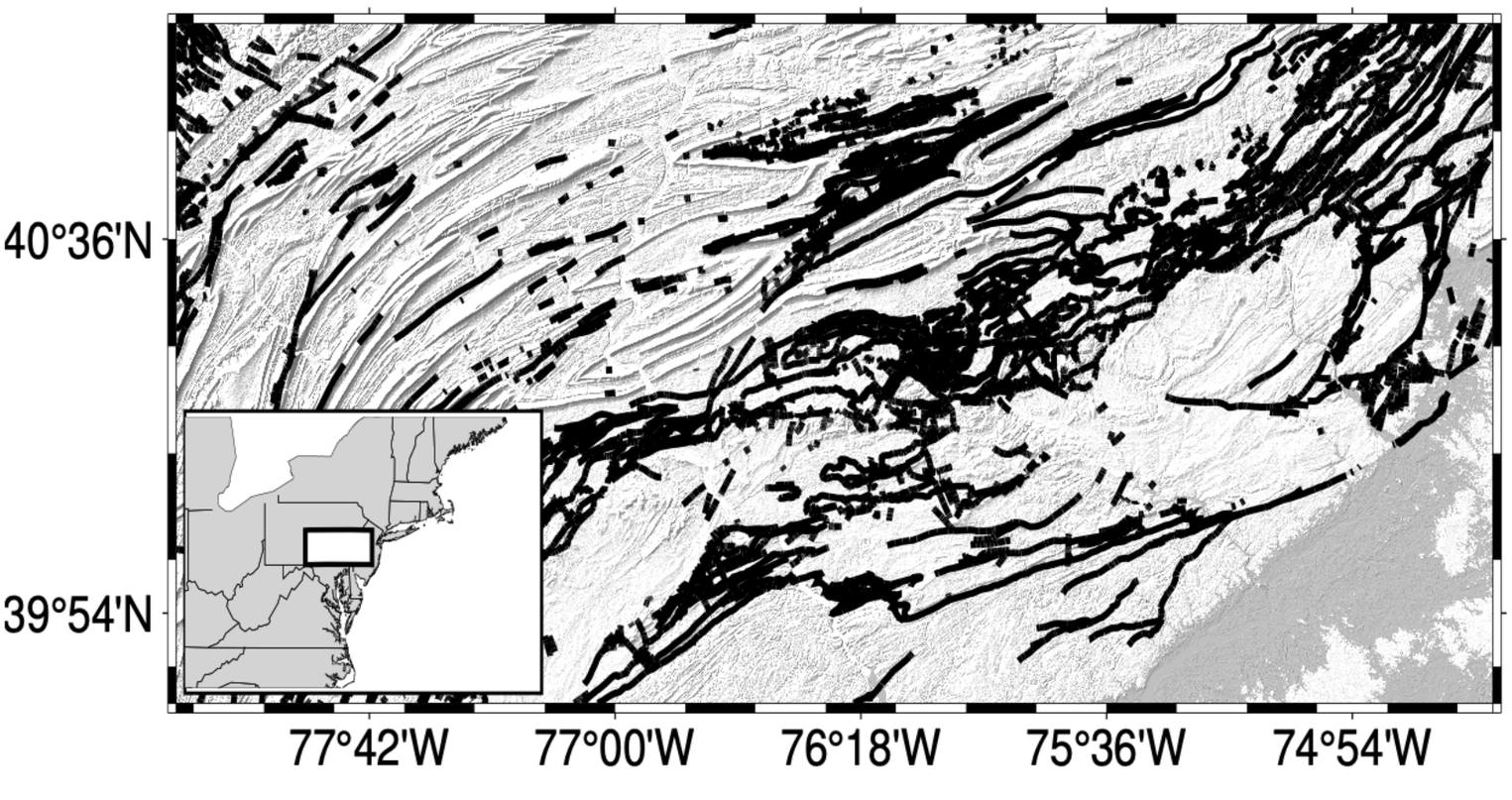
40°36'N
39°54'N
77°42'W
77°00'W
76°18'W
75°36'W
74°54'W

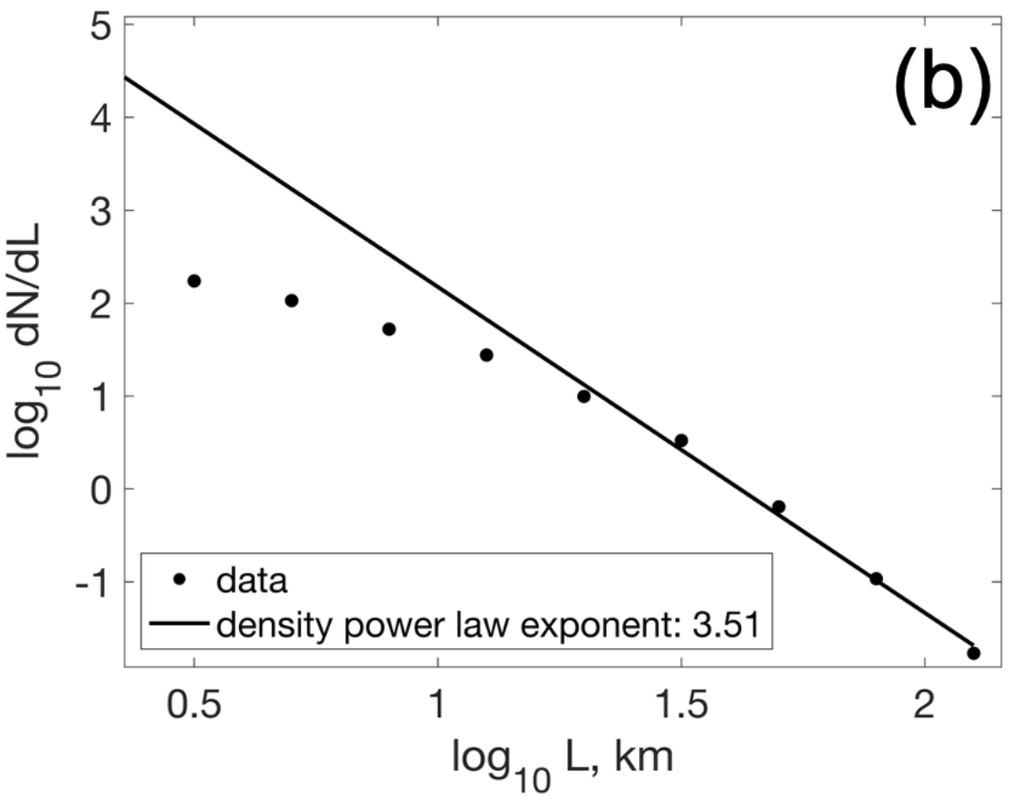
(b)
log10 dN/dL
log10 L, km
data
density power law exponent: 3.51
5
4
3
2
1
0
-1
0.5
1
1.5
2

Figure 3.

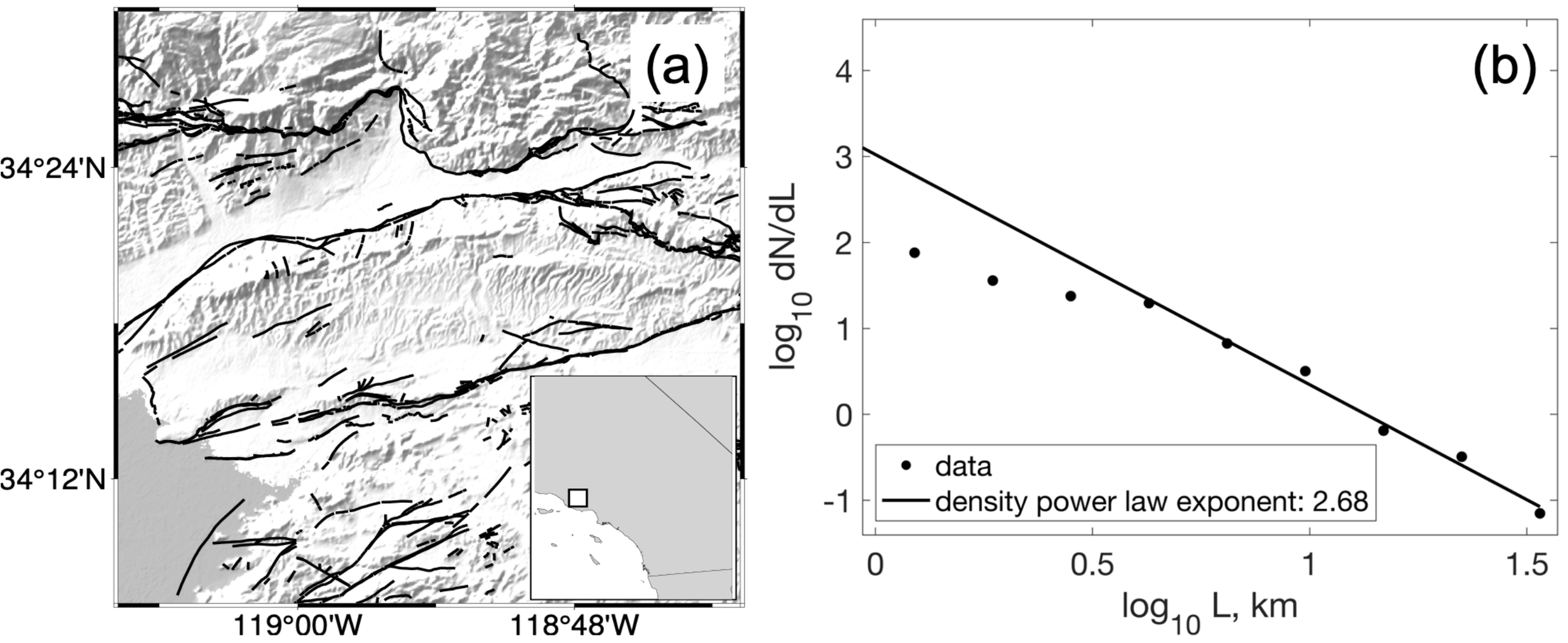
(a)
34°24'N
34°12'N
119°00'W
118°48'W
(b)
4
3
2
1
0
-1
log10 dN/dL
data
density power law exponent: 2.68
0
0.5
1
1.5
log10 L, km

Figure 4.

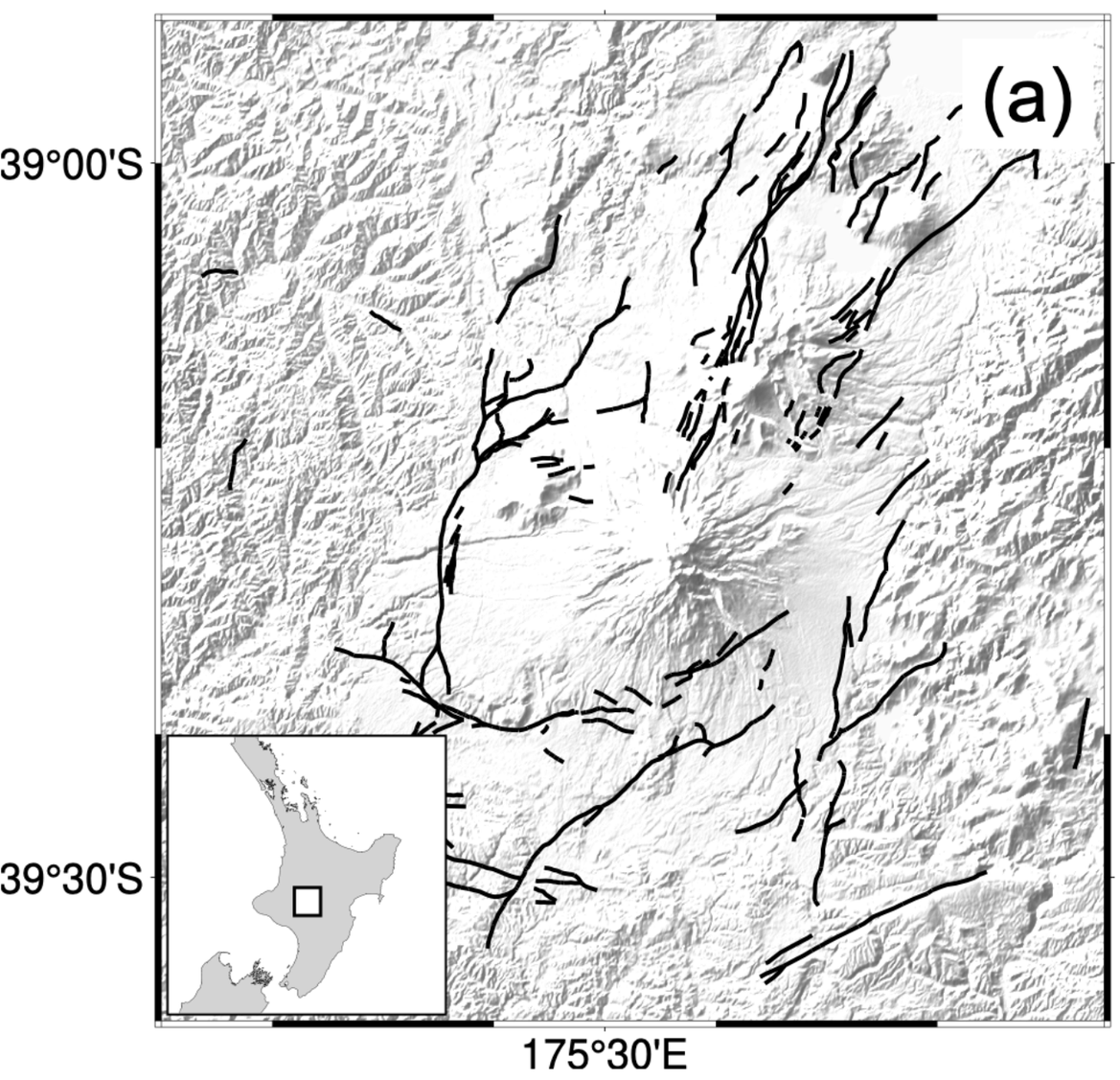
(a)
39°00'S
39°30'S
175°30'E

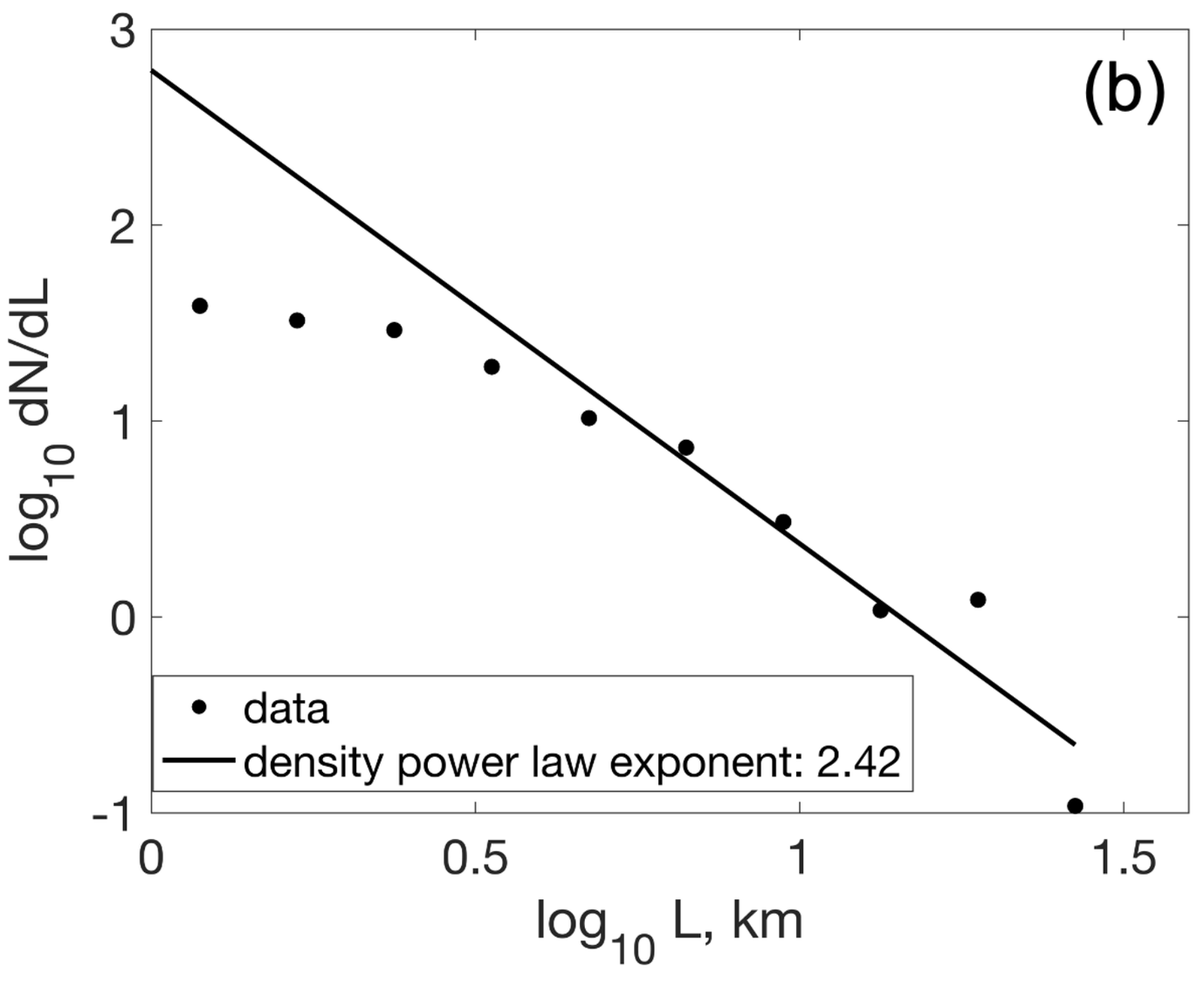
(b)
3
2
1
0
-1
0
0.5
1
1.5
log10 dN/dL
log10 L, km
data
density power law exponent: 2.42

Figure 5.

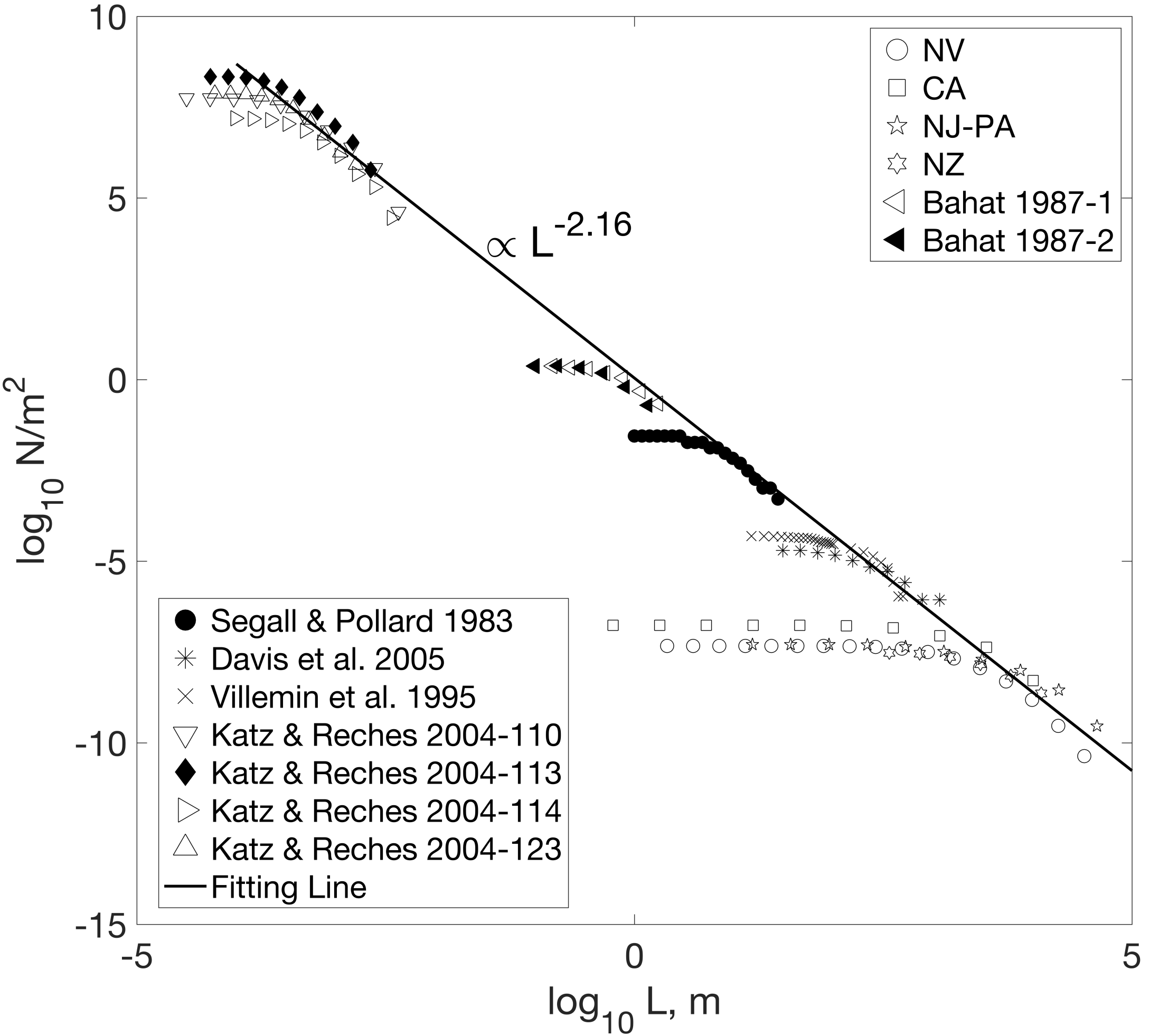
10
5
0
-5
-10
-15
-5
0
5
$\log_{10}$ N/m^2
$\log_{10}$ L, m
$\propto L^{-2.16}$
NV
CA
NJ-PA
NZ
Bahat 1987-1
Bahat 1987-2
Segall & Pollard 1983
Davis et al. 2005
Villemin et al. 1995
Katz & Reches 2004-110
Katz & Reches 2004-113
Katz & Reches 2004-114
Katz & Reches 2004-123
Fitting Line

Figure 6.

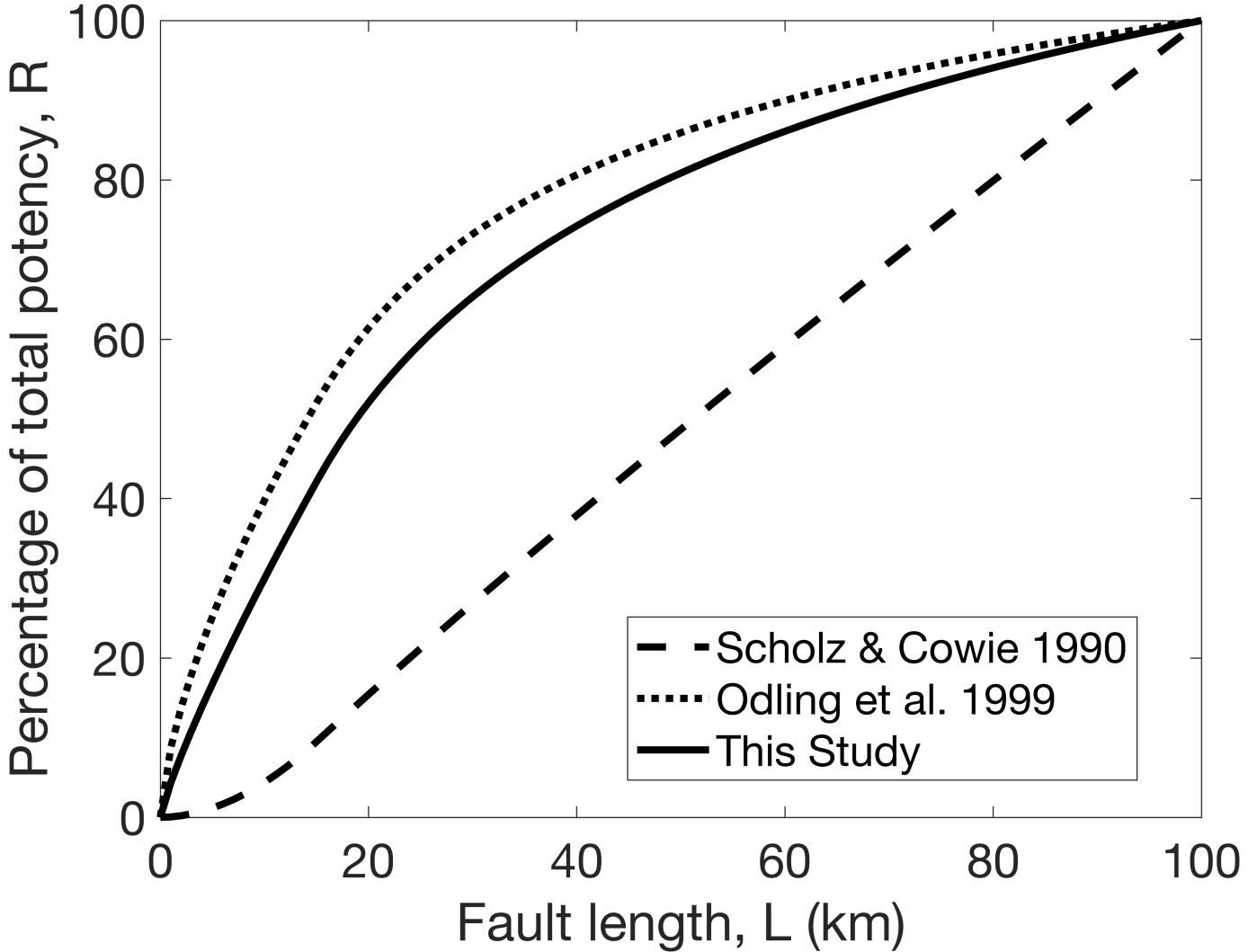
Percentage of total potency, R
Fault length, L (km)
0
20
40
60
80
100
Scholz & Cowie 1990
Odling et al. 1999
This Study

Figure 7.

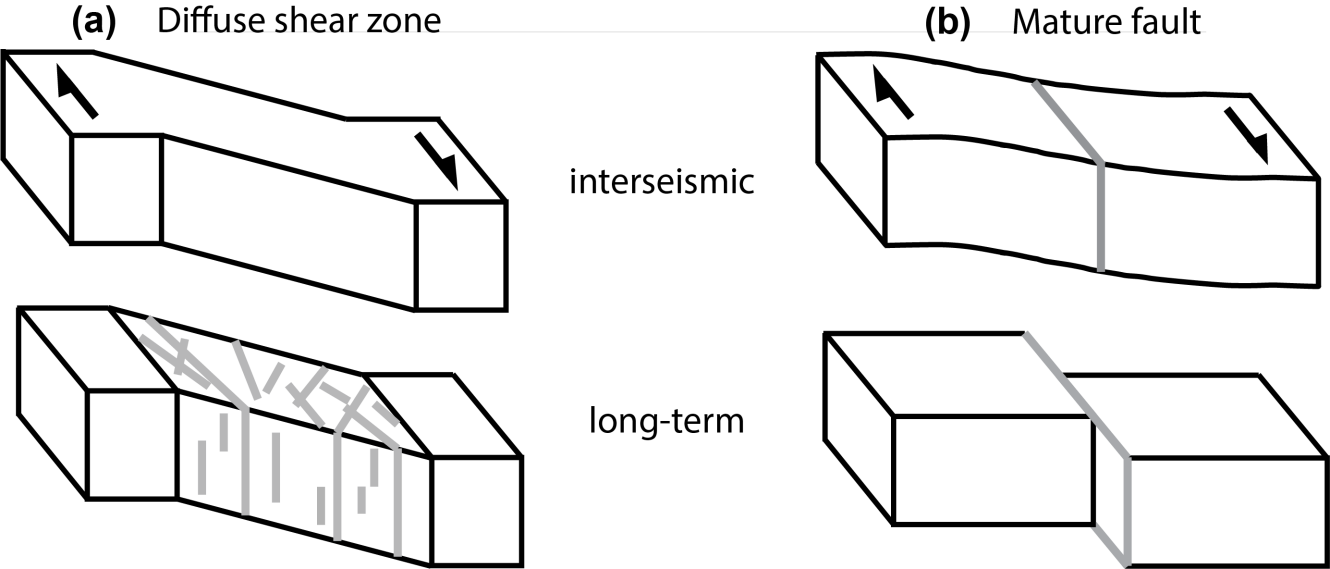
(a) Diffuse shear zone
(b) Mature fault
interseismic
long-term